RSC Advances

ROYAL SOCIETY OF CHEMISTRY

PAPER

View Article Online
View Journal | View Issue

Check for updates

Cite this: *RSC Adv.*, 2023, **13**, 26302

Tetranuclear lanthanide-based silsesquioxanes: towards a combination of a slow relaxation of the magnetization and a luminescent thermometry†

Gautier Félix,[a] Saad Sene,[a] Alena Kulakova,[abc] Alexey N. Bilyachenko,*[bc] Victor N. Khrustalev,[cd] Elena S. Shubina,[b] Yannick Guari[a] and Joulia Larionova*[a]

Received 20th July 2023
Accepted 28th August 2023

DOI: 10.1039/d3ra04901a

rsc.li/rsc-advances

Lanthanide-based silsesquioxanes constitute an emerging family of cage-like metallasilsesquioxanes with exciting optical and magnetic properties. We report here the synthesis, structures and luminescence properties of a series of tetranuclear lanthanide-silsesquioxane compounds of general formula $[NEt_4]_2[(Ph_4Si_4O_8)_2(Ln/Ln')_4(NO_3)_6(EtOH)_2(MeCN)_2]\cdot 4(MeCN)$ with different lanthanide ions (where Ln/Ln′ = Dy^{3+}/Eu^{3+} (**1**), Dy^{3+}/Tb^{3+} (**2**) and $Eu^{3+}/Tb^{3+}/Y^{3+}$ (**3**)) and investigate the impact of the lanthanide ions combination on magnetic and photo-luminescent properties. Compound **1** behaves as a field-induced Single Molecule Magnet (SMM) and presents temperature-dependent luminescence characteristics of Eu^{3+} making it an emissive thermometer working in the temperature range 293–373 K with the maximum relative sensitivity of 1.15% K^{-1} achieved at 293 K. Compounds **2** and **3** are paramagnets, which demonstrate a characteristic photoluminescence with Dy^{3+} to Tb^{3+} and Tb^{3+} to Eu^{3+} energy transfers, respectively.

Introduction

Coordination compounds made by an association of Ln^{3+} ions with different ligands attracted increasing interest in the recent decade due to both their magnetic and luminescent properties exciting not only from a fundament point of view, but also due to promising technological applications. Indeed, an important breakthrough in the field of molecular magnetism has been made by a recent discovery of mononuclear lanthanide complexes, such as dysprosium metallocenes, exhibiting Single-Molecule Magnetic (SMM) behaviour at temperatures near or even exceeding liquid nitrogen's boiling point relevant for their promising employment in future spintronic devices.[1–4] On the other hand, a temperature-dependence of the lanthanide-characteristic luminescence brought a new paradigm on the use of lanthanide-based coordination complexes as a smart emissive temperature probe at micro- and nanoscales.[5] They have great potential in a wide range of applications ranging from biology and medicine to cryogenics[5–7] because they offer high accuracy remote temperature measurements with significant spatial and thermal resolutions, as well as with a high maximal relative sensitivity (S_r > 1% K^{-1}).[8–12] These two discoveries inspired an important development in designing numerous mono- and polynuclear lanthanide-based complexes with optimized magnetic[13–18] or optical properties,[19–21] which are usually observed separately. Important work has also been done for the combination of a SMM behaviour with luminescence to design multifunctional magneto-luminescent complexes, in which their optical properties have been employed to probe the magnetic relaxation mechanisms.[22–25] Recently, an interesting strategy combining SMM behaviour with emissive thermometry has opened exciting perspectives in the temperature monitoring in future SMM-based devices at the molecular level.[25] However, the examples of SMM exhibiting temperature dependent luminescence able to work as an efficient thermometer are very scarce. We can cite, for instance, some rare examples of Dy^{3+}-,[26] Yb^{3+}-,[27,28] Tb^{3+}-,[29] Nd^{3+}-based complexes[30] and a metallofullerene $DyErScN@C_{80}$ (ref. 31) exhibiting a low temperature SMM behaviour and an emissive thermometry with, in a few rare cases, an overlap of both properties in the working temperature range.

Recently, we reported a promising family of luminescent and/or magnetic tetranuclear cage-like lanthanide-silsesquioxanes designed by a combination of lanthanide ions

---

[a] *ICGM, Univ. Montpellier, CNRS, ENSCM, Montpellier, France. E-mail: joulia.larionova@umontpellier.fr*

[b] *A. N. Nesmeyanov Institute of Organoelement Compounds of Russian Academy of Sciences, 28 Vavilova Str., 119334, Moscow, Russia. E-mail: bilyachenko@ineos.ac.ru*

[c] *Peoples' Friendship University of Russia, (RUDN University), Miklukho-Maklay Str., 6, 117198, Moscow, Russia*

[d] *Zelinsky Institute of Organic Chemistry, Russian Academy of Sciences, Leninsky Prospect 47, Moscow 119991, Russia*

† Electronic supplementary information (ESI) available: Additional structural and magnetic and *ab initio* calculations data. CCDC 2240602 (**1**), 2240603 (**2**), 2240604 (**3**). For ESI and crystallographic data in CIF or other electronic format see DOI: https://doi.org/10.1039/d3ra04901a

with the silsesquioxane repeating subunit $(RSiO_{1.5})_8$ forming the robust inorganic Si–O–Si skeleton.[32–34] We demonstrated that Dy^{3+} containing silsesquioxane of the formula $(Et_4N)_2[(PhSiO_{1.5})_8(Y_{0.75}Dy_{0.25}O_{1.5})_4(O)(NO_{2.5})_6(EtOH)_2(MeCN)_2]$ presented both, field-induced SMM behaviour and Dy^{3+} characteristic emission, while Tb^{3+} and Eu^{3+} analogues exhibit paramagnetism with a low temperature spin flip and luminescence. On the other hand, an anionic cage containing solid-state solution of mixed Tb^{3+}/Eu^{3+} lanthanides demonstrated a tuneable thermosensitive Tb^{3+}-to-Eu^{3+} energy transfer driven by the Tb^{3+} and Eu^{3+} emission, which permitted to propose it as an efficient temperature sensor with excellent linearity, repeatability and good thermal sensitivity.[34] Note that these multifunctional lanthanide silsesquioxanes demonstrated several advantages in comparison to simple coordination complexes and hybrid materials, consisting in: (i) well definite but versatile crystal structures in which the nature of lanthanide ions and terminal ligands can be modified without impacting the structural organisation. This offers an important flexibility in designing luminescent and magnetic systems because emission and excitation wavelengths can be easily adjusted; (ii) lanthanide ions are integrated inside the cage-like rigid framework through the formation of covalent bonds with bridging oxygen atoms, which preclude any lanthanides' leaching; (iii) the presence of silsesquioxane moieties offers important chemical, photo- and thermal stabilities. Moreover, it may be considered as "lanthanide molecular cluster" with promising photo-luminescence properties.[35] Remarkably, these compounds present an important stability to photobleaching at a relatively high working temperature (373 K) due to the presence of the siloxane matrix, which played a protective role. However, up to now, the combination of a SMM behaviour and the emissive thermometry has never been observed in the same silsesquioxane cage.

In the present work, we extend our approach to solid solutions of different lanthanide ions in the aims to design luminescent and magnetic cage-like silsesquioxanes with different emission colour and check their ability to work as emissive thermometers. Therefore, we report here the synthesis, crystal structures of tetranuclear lanthanide-based silsesquioxanes, $[NEt_4]_2[(Ph_4Si_4O_8)_2(Ln/Ln')_4(NO_3)_6(EtOH)_2(MeCN)_2]\cdot 4(MeCN)$ where $Ln/Ln' = Dy^{3+}/Eu^{3+}$ (**1**), Dy^{3+}/Tb^{3+} (**2**), $Eu^{3+}/Tb^{3+}/Y^{3+}$ (**3**) and investigate the contribution of these lanthanide ions on magnetic and photo-luminescent properties with a particular focus on an association of SMM properties and luminescent thermometry. The choice of Dy^{3+} ion in the couples Ln/Ln′ has been motivated by its promising ability to bring SMM behaviour due to its high magnetic anisotropy and high magnetic moment. We introduced alongside Dy^{3+} highly emissive Eu^{3+} or Tb^{3+} ions in order to combine a slow relaxation of the magnetization with a luminescence. Note also that the use of Y^{3+} permits the magnetic dilution. All of the obtained compounds present emission characteristic of constituent Ln^{3+} ions in solid state at room temperature. The cage-like silsesquioxane Dy^{3+}/Eu^{3+} **1** presents a slow relaxation of the magnetization at low temperature making it a field induced SMM and a temperature dependent emission relevant of Eu^{3+} in the temperature range between 293 and 373 K. This latter characteristic allows it to operate as an emissive thermometer with the maximum relative sensitivity of 1.15% K^{-1} achieved at 293 K, which is comparable to other promising emissive thermometers. Note that **1** is the third example of Dy^{3+} based SMM exhibiting emissive thermometry properties. Compounds Dy^{3+}/Tb^{3+} **2** and Tb^{3+}/Eu^{3+} **3** are paramagnets, which exhibit a characteristic photoluminescence with Dy^{3+} to Tb^{3+} and Tb^{3+} to Eu^{3+} energy transfers, respectively, while their emission is not temperature dependent.

Experimental

General conditions

Phenyltrimethoxysilane (98%), Et_4NCl (≥98%), $Eu(NO_3)_3\cdot 6H_2O$ (99.9% trace metals basis), $Tb(NO_3)_3\cdot 6H_2O$ (99.9% trace metals basis), $Dy(NO_3)_3\cdot 6H_2O$ (99.9% trace metals basis), $Y(NO_3)_3\cdot 6H_2O$ (99.9% trace metals basis), ethanol and acetonitrile were purchased from Merck and used as received.

Synthesis of $[NEt_4]_2[(Ph_4Si_4O_8)_2(Ln/Ln')_4(NO_3)_6(EtOH)_2(MeCN)_2]\cdot 4(MeCN)$ Ln = Eu^{3+}/Dy^{3+} 1, Dy^{3+}/Tb^{3+} 2, $Eu^{3+}/Tb^{3+}/Y^{3+}$ 3

The synthesis of compounds **1–3** has been performed in a similar way. A mixture of $PhSi(OMe)_3$ (0.94 mmol) and NaOH (0.94 mmol) was dissolved in 30 mL of ethanol. The resulting solution was heated to reflux for 1.0 h. Afterwards the mixture of lanthanide salts (0.47 mmol in total, see amount of each lanthanide salt below) and Et_4NCl (0.47 mmol) dissolved in 30 mL of CH_3CN were added at once. The resulted mixture was heated to reflux for 3 h and the solution was filtered from the insoluble residue providing a colourless solution. Crystalline materials were obtained by slow evaporation of solvents in a period of a few days. The single crystals suitable for a single crystal X-ray diffraction were collected. The products were dried in vacuum to perform elemental analysis and to calculate the yield.

$[NEt_4]_2[(Ph_4Si_4O_8)_2Dy_{0.87}Eu_{3.12}(NO_3)_6(EtOH)(MeCN)_2]\cdot 4MeCN$ 1. Reactants loadings: $PhSi(OMe)_3$ (0.186 g, 0.94 mmol), NaOH (0.038 g, 0.94 mmol), $Eu(NO_3)_3\cdot 6H_2O$ (0.16 g, 0.35 mmol), $Dy(NO_3)_3\cdot 6H_2O$ (0.05 g, 0.12 mmol), Et_4NCl (0.08 g, 0.47 mmol). Yield = 33% (0.09 g).

Anal. calcd (for the theoretical Eu_3Dy-compound): % Dy, 6.92; Eu, 19.41; Si, 9.57. Found (for $Eu_{3.12}Dy_{0.87}$-compound): % Dy, 6.03; Eu, 20.21; Si, 9.58.

$[NEt_4]_2[(Ph_4Si_4O_8)_2Dy_{3.12}Tb_{0.88}(NO_3)_6(EtOH)_2(MeCN)_2]\cdot 4MeCN$ 2. Reactants loadings: $PhSi(OMe)_3$ (0.186 g, 0.94 mmol), NaOH (0.038 g, 0.94 mmol), $Dy(NO_3)_3\cdot 6H_2O$ (0.16 g, 0.35 mmol), $Tb(NO_3)_3\cdot 6H_2O$ (0.05 g, 0.12 mmol), Et_4NCl (0.08 g, 0.47 mmol). Yield = 40% (0.11 g).

Anal. calcd (for the theoretical Dy_3Tb-compound): % Dy, 20.51; Si, 9.45; Tb, 6.69. Found (for the $Dy_{3.12}Tb_{0.88}$-compound): % Dy, 21.33; Si, 9.45; Tb, 5.88.

$[NEt_4]_2[(Ph_4Si_4O_8)_2Eu_{0.87}Tb_{1.01}Y_{2.11}(NO_3)_6(EtOH)_2(MeCN)_2]\cdot 2EtOH$ 3. Reactants loadings: $PhSi(OMe)_3$ (0.186 g, 0.94 mmol), NaOH (0.038 g, 0.94 mmol), $Y(NO_3)_3\cdot 6H_2O$ (0.09 g, 0.23 mmol),

$Eu(NO_3)_3\cdot 6H_2O$ (0.05 g, 0.12 mmol), $Tb(NO_3)_3\cdot 6H_2O$ (0.05 g, 0.12 mmol), Et_4NCl (0.08 g, 0.47 mmol). Yield = 42% (0.11 g).

Anal. calcd (for the theoretical $EuTbY_2$-compound): % Eu, 6.85; Si, 10.13; Tb, 7.16; Y, 8.01. Found (for the $Eu_{0.87}Tb_{1.01}Y_{2.11}$-compound): % Eu, 5.89; Si, 10.17; Tb, 7.26; Y, 8.49.

X-ray crystallography

X-ray diffraction data for **1–3** were collected on a four-circle Rigaku Synergy S diffractometer equipped with a HyPix6000HE detector ($T = 100$ K, λ(MoKα)-radiation, kappa geometry, shutterless φ and ω-scan mode). The data were integrated and corrected for absorption by the CrysAlisPro program.[36] For details, see Table S1.† The structures were solved by a direct method and refined by full-matrix least squares technique on F^2 with anisotropic displacement parameters for non-hydrogen atoms. All attempts to model and refine positions of the acetonitrile solvate molecules in **3** were unsuccessful. Therefore, their contribution to the total scattering pattern was removed by use of the utility *SQUEEZE* in PLATON15.[37] The hydrogen atoms of the OH-groups were localized in the difference-Fourier maps and refined isotropically with fixed displacement parameters [$U_{iso}(H) = 1.5U_{eq}(O)$]. The other hydrogen atoms were placed in calculated positions and refined within riding model with fixed isotropic displacement parameters [$U_{iso}(H) = 1.5U_{eq}(C)$ for the CH_3-groups and $1.2U_{eq}(C)$ for the other groups]. All calculations were carried out using the SHELXTL program suite.[38]

Crystallographic data have been deposited with the Cambridge Crystallographic Data Centre, CCDC 2240602 (**1**), CCDC 2240603 (**2**), CCDC 2240604 (**3**).

Crystal structure determination was performed in the Department of Structural Studies of Zelinsky Institute of Organic Chemistry, Moscow, Russia.

Characterizations

IR spectra (KBr pellets) were recorded using PerkinElmer Spectrum Two FT-IR Spectrometer. Compounds exhibit the similar set of signals: 1600–1400 cm^{-1} (νC=C, νC=N) 1130 cm^{-1} (νPh–Si), 945–1060 cm^{-1} (νasSi–O, νasSi–O–Si), 750–680 cm^{-1} (σC–H of mono-substituted phenyl group). The quantifications of lanthanides and Si elements were performed by using scanning electron microscope and energy dispersive X-ray analysis (SEM-EDX) on a FEI Quanta FEG 200 instrument. The powders were deposited on an adhesive carbon film and analysed under vacuum. The quantification of the heavy elements was carried out with the INCA software, with a dwell time of 3 μs.

The emission and excitation spectra were evaluated in solid state (powders) at room (298 K) and low (77 K) temperatures using a spectrofluorimeter Edinburgh FLS-920 by using a 450 W Xe arc lamp as the excitation source. The spectra were corrected for detection and optical spectral response of the spectrofluorimeter. The photoluminescent measurements as a function of temperature were done in solid state by using the temperature setup incorporated in the Edinburgh spectrofluorimeter. The emission spectra were recorded in the temperature range from 293 to 373 K. At each temperature step, a period of 2 min was given to allow the temperature to stabilize, and then 5 emission spectra were recorded with a dwell time of 0.3 s and a step of 1 nm. Magnetic susceptibility data were collected with a Quantum Design MPMS-XL SQUID magnetometer working between 1.8 and 350 K with the magnetic field up to 7 T. The sample was prepared in ambient condition. The data were corrected for the sample holder and the diamagnetic contributions calculated from the Pascal's constants.

Results and discussions

Synthesis and crystal structures

The synthetic strategy implies the formation of tetranuclear anionic cage-like silsesquioxanes $[(Ph_4Si_4O_8)_2(Ln/Ln')_4(NO_3)_4(OH)(EtOH)_3(H_2O)]^{2-}$ in association with a relatively bulky $(NEt_4)^+$ non-coordinating cation. A series of complexes $[NEt_4]_2[(Ph_4Si_4O_8)_2(Ln/Ln')_4(NO_3)_6(EtOH)_2(MeCN)_2]\cdot 4(MeCN)$, where Ln/Ln′ = Dy^{3+}/Eu^{3+} **1**, Dy^{3+}/Tb^{3+} **2**, $Eu^{3+}/Tb^{3+}/Y^{3+}$ **3**, were synthesized by employing a two-step approach. First, the *in situ* formation of $[PhSi(O)ONa]_x$ moiety with their further reaction with Et_4NCl salt and the corresponding Ln^{3+} salts. The SEM-EDX and the elemental analysis permitted to determine the composition of compounds **1–3**.

Single crystals X-ray diffraction analysis performed on compounds **1–3** revealed that they are isostructural and crystallize in the $P\bar{1}$ space groups (Table S1, ESI†). Their crystal structures are similar to the previously published tetranuclear cage-like silsesquioxanes $[Cat]_2[(Ph_4Si_4O_8)_2(Ln)(NO_3)_6(EtOH)_2(MeCN)_2]\cdot solv$ (where Ln = Tb, Eu and Dy).[32–34] The crystal structure of **1** is described in details (Fig. 1) and the ones of **2** and **3** are shown in Fig. S1 and S2, ESI† and the crystallographic parameters are gathered in Tables S1 and S2, ESI.†

The crystal packing of compound **1** may be described as an assembly of di-anionic tetranuclear lanthanide-germanoxane molecules along the *c* axis alternated with NEt_4^+ cations. The unit cell possesses two motives with two different units arranged perpendicular to each other (Fig. 1a). The shortest intermolecular Eu/Dy⋯Eu/Dy distance is equal to 12.628 Å. The molecular structure of **1** may be described as a prism made by eight Si atoms comprising the $Dy_{0.87}Eu_{3.12}O_8$ core in the middle providing an appearance of a new year paper lantern to the molecule (Fig. 1b and c). In this lanthanide-based core, each Dy^{3+}/Eu^{3+} ion is linked to two others through two bridging oxygen atoms to form a distorted square (Fig. 1d). There are two different eight-coordinated Dy/Eu sites, which adopt a distorted square antiprismatic geometry (Fig. 1d). In two of theme, lanthanide atoms are coordinated by four bridging oxygen atoms from the core and four oxygen atoms from two terminal bidentate nitrate ligands, while in two others, Dy/Eu is linked to four bridging oxygens, two terminal oxygens from one nitrate, one ethanol and one acetonitrile molecules. The (Dy/Eu)–O distances are in the range 2.310(9)–2.563(3) Å, while the (Dy/Eu)–N one is equal to 2.551(4) and 2.5514(10) Å. The O–(Dy/Eu)–O angles in the square are equal to 71.62 and 72.90°. (Table S2, ESI†). The intramolecular Dy/Eu⋯Dy/Eu distances in the

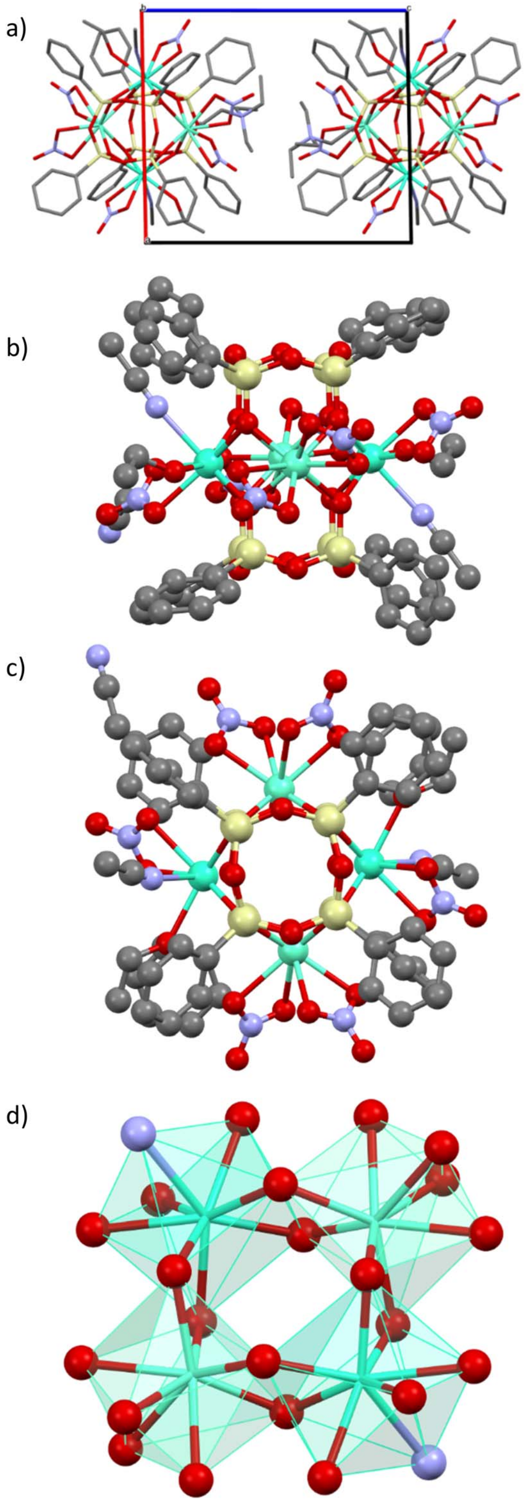

Fig. 1 (a) Perspective view of the crystal packing for **1** along the crystallographic axis *b*; (b) and (c) molecular structure of **1** showing the prism-like polyhedron in the form of a new year paper lantern; (d) polyhedron of Dy/Eu atoms in the $(Dy_{0.92}/Eu_{3.08}O_8)O$ core. Colour code: light green Dy/Eu; light yellow Si; red O; blue N; grey C. Hydrogen atoms and crystallized acetonitrile molecules have been omitted for clarity.

square are equal to 3.724 and 3.773 Å, which indicates that lanthanides are relatively close.

Magnetic properties

The magnetic properties of compounds **1–3**, were investigated with a SQUID MPMS3 magnetometer working between 1.8 and 310 K up to 7 T. The temperature dependences of the magnetic susceptibility performed in direct current (dc) mode were performed under an applied magnetic field of 1000 Oe. At room temperature, the χT values are in a relatively good agreement with the expected theoretical values (see Table S3, ESI†). The χT product decreases as the temperature decreases, which reflects the thermal depopulation of the m_J levels and/or the presence of antiferromagnetic interactions between the lanthanide ions (Fig. 2a).

The field dependences of the magnetization performed at 1.8 K show a linear and a rapid increase of the magnetization in the low field region and then a slow increase after 1 tesla. But the saturation is not reached at 7 tesla, which indicates the presence of a significant magnetic anisotropy, as usually observed in lanthanide-based complexes (Fig. 2b).

The dynamic measurements in the ac mode have been performed for all compounds, but only sample **1** demonstrated a slow relaxation of the magnetization. This fact may be explained by the presence of magnetic interactions between

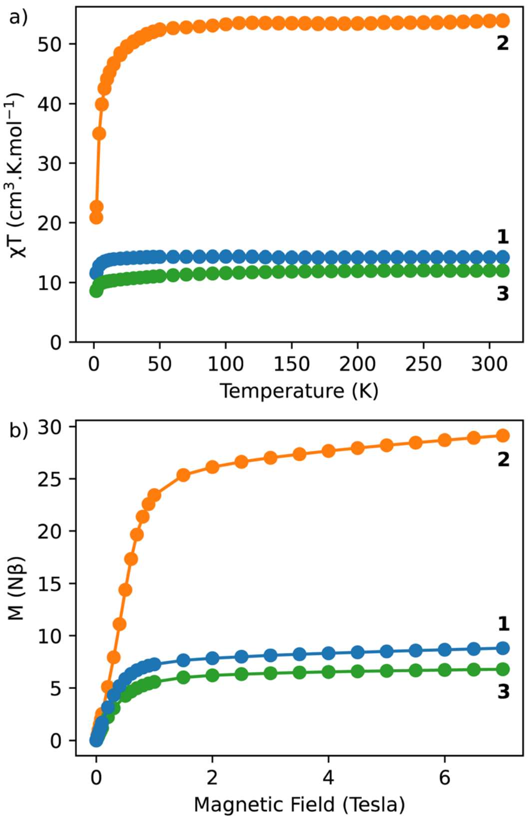

Fig. 2 (a) χT *vs.* T curves performed under an applied magnetic field of 1000 Oe for **1–3**; (b) magnetization *vs.* field curves obtained at 1.8 K for **1–3**.

Dy^{3+} in **2**, which negatively affects the relaxation dynamics.[18,33] For **1**, the in-phase, χ', and the out-of-phase, χ'', components of the ac susceptibility does not present an important signal under a zero-dc field, which may be ascribed to the presence of the fast Quantum Tunnelling of the Magnetization (QTM). In order to avoid its influence, the frequency dependence of the ac susceptibility was measured under different applied dc fields, which shows an appearance of a signal for both components under an applied field (Fig. S3, ESI†). The temperature and the field dependences of the relaxation time can be fitted by using the eqn (1):[39]

$$\tau^{-1} = AH^4T + \frac{B_1}{1+B_2H^2} + \tau_0^{-1}\exp\left(-\frac{\Delta}{k_\mathrm{B}T}\right) + CT^\mathrm{m}, \tag{1}$$

where the first, second, third and fourth terms represent the relaxation time for the direct, QTM, Orbach and Raman processes, respectively (Fig. 3). To avoid the over parametrization, the eqn (1) can be rewritten into eqn (2):

$$\tau^{-1} = AH^4T + \frac{B_1}{1+B_2H^2} + C_\mathrm{T}, \tag{2}$$

where C_T is a term corresponding to possible Orbach and Raman processes, which depends on temperature but does not depend on magnetic field. The obtained fit values are $C_\mathrm{T} = 672 \pm 12\ \mathrm{s}^{-1}$, $A = (6.71 \pm 0.85) \times 10^4\ \mathrm{s}^{-1}\ \mathrm{T}^{-4}\ \mathrm{K}^{-1}$, $B_1 = (3.05 \pm 0.41) \times 10^3\ \mathrm{s}^{-1}$ and $B_2 = (1.37 \pm 0.32) \times 10^4\ \mathrm{T}^{-2}$. The fitting of the field dependence of the relaxation time with eqn (2) permitted to determine the optimum magnetic field of 1000 Oe, which corresponds to the higher relaxation time (Fig. S3d†).

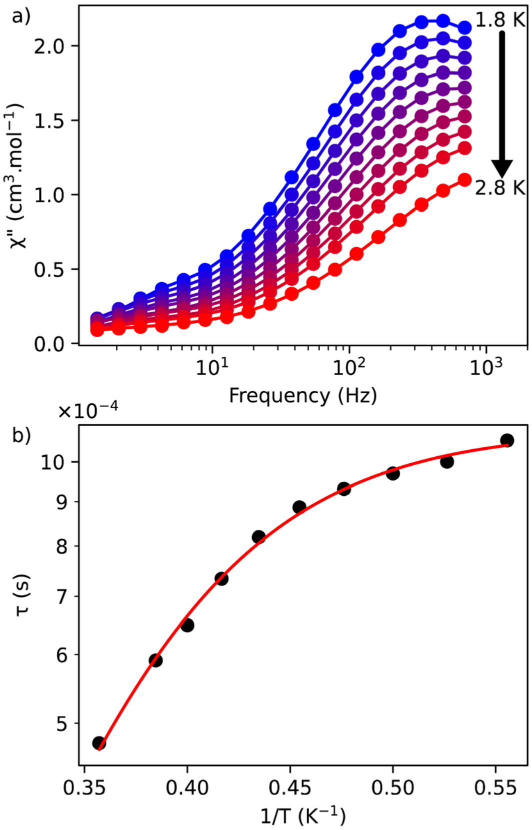

Fig. 3 (a) Out-of-phase, χ'', component of the ac magnetic susceptibility as a function of frequency at different temperatures measured under an optimal dc field of 1000 Oe for **1**; (b) temperature dependence of the relaxation time for **1** under 1000 Oe. The red solid line represents the fits done by using the eqn (3).

The frequency dependence of the ac susceptibility under the optimal field of 1000 Oe reveals the presence of a series of peaks, for which the maxima shift towards higher frequencies as the temperature increases, suggesting the occurrence of a field-induced slow relaxation of the magnetization (Fig. 3a, S4a and b†). Eqn (3) can be rewritten from the eqn (1) to avoid the over parametrisation:

$$\tau^{-1} = \tau_0^{-1}\exp\left(-\frac{\Delta}{k_\mathrm{B}T}\right) + C_\mathrm{H}, \tag{3}$$

where C_H is a term which takes into account QTM and which depends on magnetic field but is constant as a function of temperature. Several combinations of the relaxation time as a function of the temperature were tested, and only the one corresponding to eqn (3) was relevant. The obtained value of the effective energy barrier, Δ, is equal to $11.3 \pm 0.6\ \mathrm{cm}^{-1}$ with $\tau_0 = (2.5 \pm 0.8) \times 10^{-6}$ s. The obtained value of C_H is equal to $901 \pm 22\ \mathrm{s}^{-1}$ (Fig. 3b). The analysis of the dynamic magnetic properties therefore indicates that compound **1** is a field-induced SMM in which the QTM process can be partially supressed by an application of the magnetic field.

Photoluminescence investigations

The photoluminescence of **1–3** was investigated in solid-state at room temperature (298 K). All compounds exhibit the typical Ln^{3+}-characteristic emissions.

Luminescence of Dy^{3+}/Eu^{3+} containing compound 1

The excitation spectrum of Dy^{3+}/Eu^{3+} containing compound **1** were recorded by monitoring the main emission of Eu^{3+} at 612 nm ($^5D_0 \rightarrow {}^7F_2$) (Fig. 4a). A series of narrow lines appeared that can be attributed to transitions between $^7F_0$ and different excited states indicating that Eu^{3+} is populated through a direct excitation into the intra-$4f^8$ lines and that the antenna effect is not operational in this case. The excitation spectrum recorded with the main emission of Dy^{3+} expected at around 570 nm did not reveal the bands characteristic for this ion.

The emission spectrum of **1** at room temperature recorded under excitation at 395 nm exhibit a series of classical Eu^{3+} $^5D_0 \rightarrow {}^7F_{0-4}$ characteristic emission lines with the most intense red emission centred at 612 nm corresponding to $^5D_0 \rightarrow {}^7F_2$ transition (Fig. 4b). The very weak $^5D_0 \rightarrow {}^7F_0$ transition observed at 580 nm confirms the low symmetry of the coordination environment of the Eu^{3+} sites.[40] The complicated profile of the $^5D_0 \rightarrow {}^7F_1$ transition (several components) is in agreement with the presence of two europium sites in distorted square antiprismatic geometry. As expected for compounds with a relatively low symmetry of Eu sites, the main transition provides a red $^5D_0 \rightarrow {}^7F_2$ emission. Moreover, since the transitions $^5D_0 \rightarrow {}^7F_2$ and $^5D_0 \rightarrow {}^7F_4$ are very sensitive to the coordination environment of the Eu site, their splitting in six or five

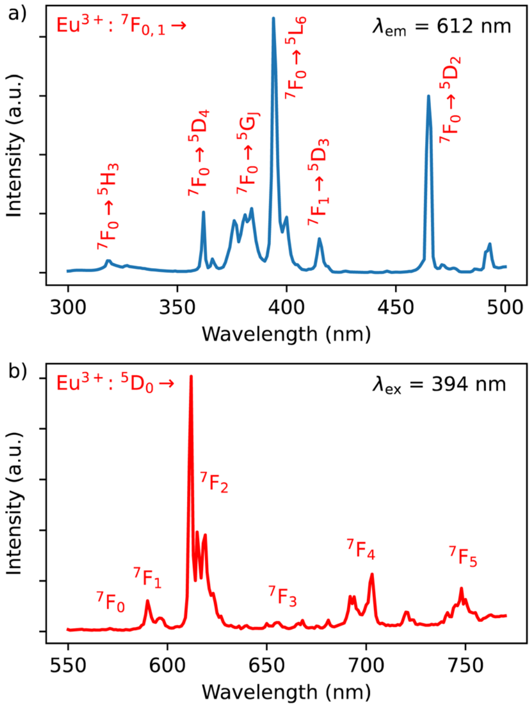

Fig. 4 (a) Excitation spectrum of **1** monitored at $\lambda_{em} = 612$ nm (top) in solid state at room temperature; (b) emission spectrum of **1** performed with $\lambda_{ex} = 394$ nm in solid state at room temperature.

components, respectively, is not surprising.[40] Note that the direct excitation in the expected Dy^{3+} related transitions (for instance in the $^6H_{15/2} \rightarrow {}^4I_{15/2}$ transition expected at 450 nm) did not provide the appearance of the Dy^{3+} characteristic emission, which can be explained by the Eu/Dy ratio = 3.6 and high Eu^{3+} emission intensity in comparison with the Dy^{3+} ion.

In order to investigate the possibility to use Dy^{3+}/Eu^{3+} compound **1** as an emissive thermometer, we adapted an optical thermometry approach involving the temperature dependence of the thermal population of low-lying levels of Eu^{3+} situated just above the ground level.[41] The population of electronic configuration states follows the Boltzmann statistic:

$$N_j = N\frac{g_j \exp\left(-\dfrac{\Delta E_j}{k_B T}\right)}{\sum\limits_i g_i \exp\left(-\dfrac{\Delta E_i}{k_B T}\right)} \tag{4}$$

The partition function of the system is:

$$Z = \sum_i g_i \exp\left(-\frac{\Delta E_i}{k_B T}\right), \tag{5}$$

where ΔE_i is the energy difference between the level i and the ground level, g_i is the degeneracy of the level i. In the case of Eu^{3+}, the quantity of electronic configuration in the state ^7F_J is defined as:

$$N_{^7F_J}(T) = N\frac{g_{^7F_J} \exp\left(-\dfrac{\Delta E_{^7F_J}}{k_B T}\right)}{Z(T)} \tag{6}$$

It depends on the partition function, the energy level, the degeneracy of the state and the temperature. The partition function is also temperature dependent. If electronic configurations are excited from the ^7F_J state to the $^5D_0$ state, then the luminescence intensity $I_{^7F_J}(T)$ will be proportional to $N_{^7F_J}(T)$:

$$I_{^7F_J}(T) \propto N_{^7F_J}(T) \tag{7}$$

In the considered thermometry mechanism, we monitor the temperature profiles of the $^5D_0 \rightarrow {}^7F_4$ emissions obtained by using two direct excitations, $^7F_1 \rightarrow {}^5D_0$ and $^7F_2 \rightarrow {}^5D_0$ (Fig. 5d). The luminescence intensity ratio (LIR) between these emissions can be written as:

$$\mathrm{LIR}(T) = \frac{I_{^7F_2}(T)}{I_{^7F_1}(T)} = C\exp\left(-\frac{E_{^7F_2} - E_{^7F_1}}{k_B T}\right) = C\exp\left(-\frac{\Delta E}{k_B T}\right) \tag{8}$$

where C is a constant, which depends on the degeneracy and ΔE is the energy difference between $^7F_1$ and $^7F_2$.

The emission spectra of **1** measured under excitations at 590 ($^7F_1 \rightarrow {}^5D_0$) and 612 nm ($^7F_2 \rightarrow {}^5D_0$) in the temperature range 293–353 K are shown in Fig. 5a and b and the corresponding luminescence intensities at 703 nm (transition $^5D_0 \rightarrow {}^7F_4$) as a function of temperature is exhibited in Fig. 5c. As expected, the integrated intensity of the $^5D_0 \rightarrow {}^7F_4$ transition (the integrated area is 670–730 nm) under excitation at 590 nm increases with temperature, then decreases, while the one under the excitation at 612 nm (the integrated area is 670–730 nm) increases constantly. The temperature dependence of their LIR(I_1/I_2) shown in Fig. 5e is fitted with eqn (8) providing the optimized parameters $\Delta E = 686 \pm 24$ cm^{-1} and $C = 14.5 \pm 1.5$. Note that the former obtained value of ΔE is comparable to the expected one of 609 cm^{-1}.

The relative thermal sensitivity (S_r) is the parameter allowing the comparison of thermometric performances among different types of thermometers.[42] The S_r value represents the variation of the experimental parameter (LIR in the present case) per degree of temperature, expressed as:

$$S_r(T) = |\partial \mathrm{LIR}(T)/\partial T|/\mathrm{LIR}(T) \tag{9}$$

The temperature dependence of S_r is shown in Fig. 5f. The maximum S_r value is equal to 1.15% K^{-1} at 293 K. It is close to a frequently considered high relative thermal sensitivity (~1% K^{-1}),[9] and in proximity with the best S_r values reported for mixed Eu^{3+}/Tb^{3+} compounds.[43]

Luminescence of Tb^{3+}/Dy^{3+} compound 2

The Dy^{3+} ion is a well-known sensitizer to activate Tb^{3+} ions in doped glasses because the $^5D_4$ level of Tb^{3+} can be populated by the $^4F_{9/2}$ level of Dy^{3+} through energy transfer.[44–46] However, this phenomenon has been relatively scarcely exploited in molecular complexes. The excitation spectra of Tb^{3+}/Dy^{3+} containing compound **2** was monitored at room temperature within: (a) the main $^5D_4 \rightarrow {}^7F_5$ transition of Tb^{3+} at 543 nm, and (b) the $^4F_{9/2} \rightarrow {}^6H_{13/2}$ transition of Dy^{3+} at 572 nm. As shown in Fig. 6a, the excitation spectrum recorded under 543 nm emission

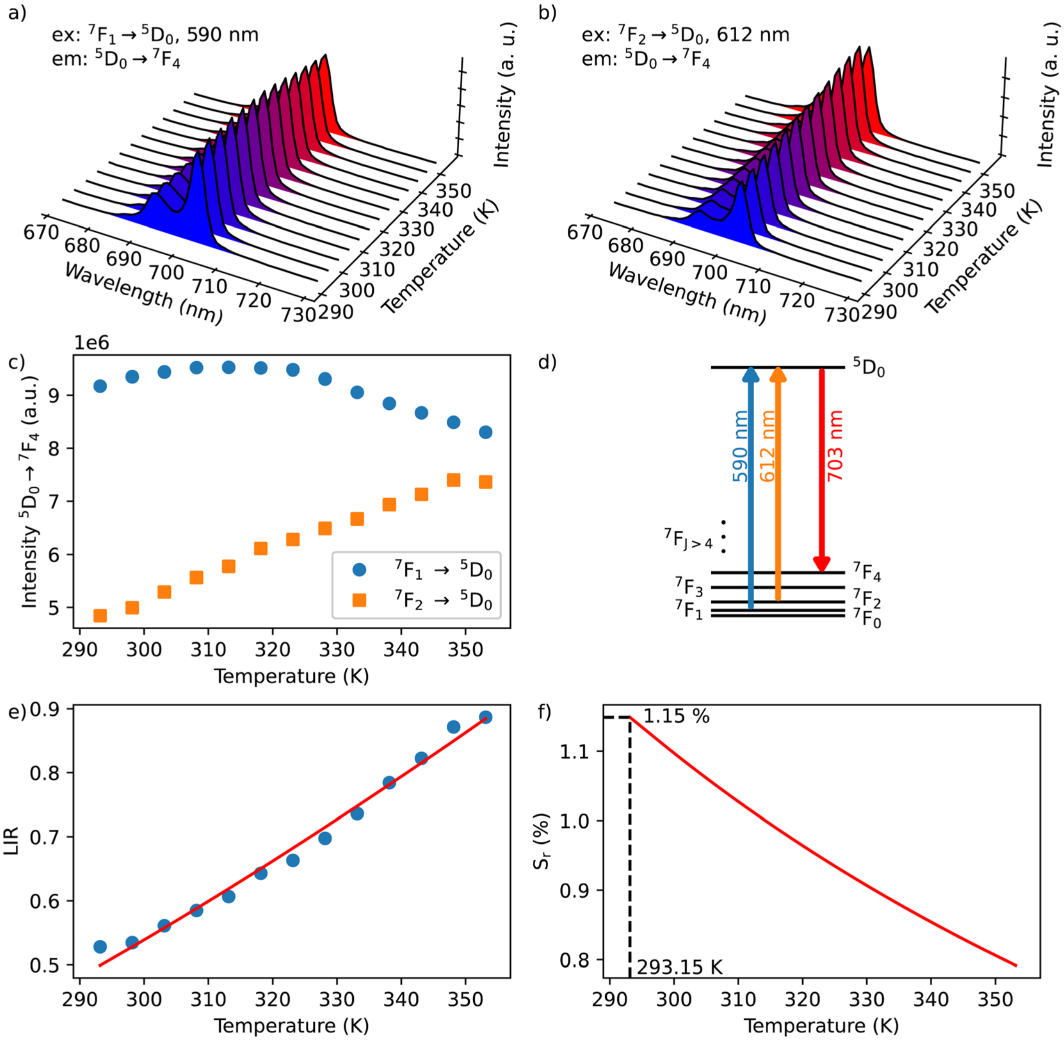

Fig. 5 Emission spectra for **1** performed in the 293 to 373 K temperature range in solid state under excitation at $\lambda_{ex} = 590$ nm (a) and at 612 nm (b); (c) temperature dependences of $^5D_0 \rightarrow {}^7F_4$ transition upon 590 ($^7F_1 \rightarrow {}^5D_0$) and 612 nm ($^7F_2 \rightarrow {}^5D_0$) excitations; (d) simplified energy diagram showing transitions excited from $^7F_{2,1}$ to $^5D_0$ and corresponding emission originating from $^5D_0$ to $^7F_4$ used for thermometry measurements; (e) normalized luminescence intensity ratio (LIR) at 700 nm monitored under excitations at 612 and 590 nm (LIR, $I_{700}Ex_{612}/I_{700}Ex_{590}$) as a function of temperature (circles) and the associated fit (red curve); (f) temperature dependence of the thermal sensitivity (S_r) for **1** showing a maximum value of 1.15% K^{-1} at 293 K.

wavelength of Tb^{3+} shows ten excitation bands among which six are assigned to Tb^{3+} ($^7F_6 \rightarrow {}^5H_7$, $^5L_{7,8}$, $^5H_7$, $^5L_9$, $^5L_{10}$, $^5G_6$ shown in green colour) and four are attributed to Dy^{3+} ion ($^6H_{15/2} \rightarrow {}^6P_{3/2}$, $^4I_{13/2}$, $^4G_{11/2}$, $^4I_{5/2}$ shown in blue colour).[32,33,44] The presence of excitation bands due to Dy^{3+} ion under the monitoring of the emission wavelength of Tb^{3+} indicates the presence of the Dy^{3+} to Tb^{3+} energy transfer. The excitation spectrum monitored at 572 nm (Dy^{3+} emission) exhibits similar transitions, while the intensities related to the Tb^{3+} transitions are lower, which could be explained by the back energy transfer (Fig. 6c).

The solid-state emission spectrum of **2** at room temperature recorded under excitation at the most intense band at 350 nm exhibits six emission bands among which four of them can be attributed to Tb^{3+} $^5D_4 \rightarrow {}^7F_{6-3}$ characteristic transitions with the main $^5D_4 \rightarrow {}^7F_5$ one centred at 543 nm and two of them correspond to Dy^{3+} transitions $^4F_{9/2} \rightarrow {}^6H_{15/2}$, $^6H_{13/2}$ (Fig. 6b). In order to demonstrate the presence of the Dy^{3+} to Tb^{3+} energy transfer, the excitation was performed in the $^6H_{15/2} \rightarrow {}^4I_{5/2}$ Dy^{3+} transition at 452 nm. The emission spectrum demonstrating the presence of characteristic Dy^{3+} bands along with the Tb^{3+} transitions, which is dominated by a main band assigned to the $^5D_4 \rightarrow {}^7F_5$ Tb^{3+} transition is shown in Fig. 6d. This signifies the energy transmission from Dy^{3+} to Tb^{3+} ions. Note that the intramolecular energy transfer between Dy^{3+} and Tb^{3+} has not been frequently demonstrated in coordination compounds of lanthanide ions, but its presence is not surprising considering that the shortest direct Ln^{3+}–Ln^{3+} distance in **2** is equal to 3.648(2) Å. The corresponding simplified energy diagram showing the Dy^{3+} to Tb^{3+} energy transfer is shown Fig. 7. Note that compound **2** does not exhibit a temperature dependence of its emission allowing to use it for emissive thermometry.

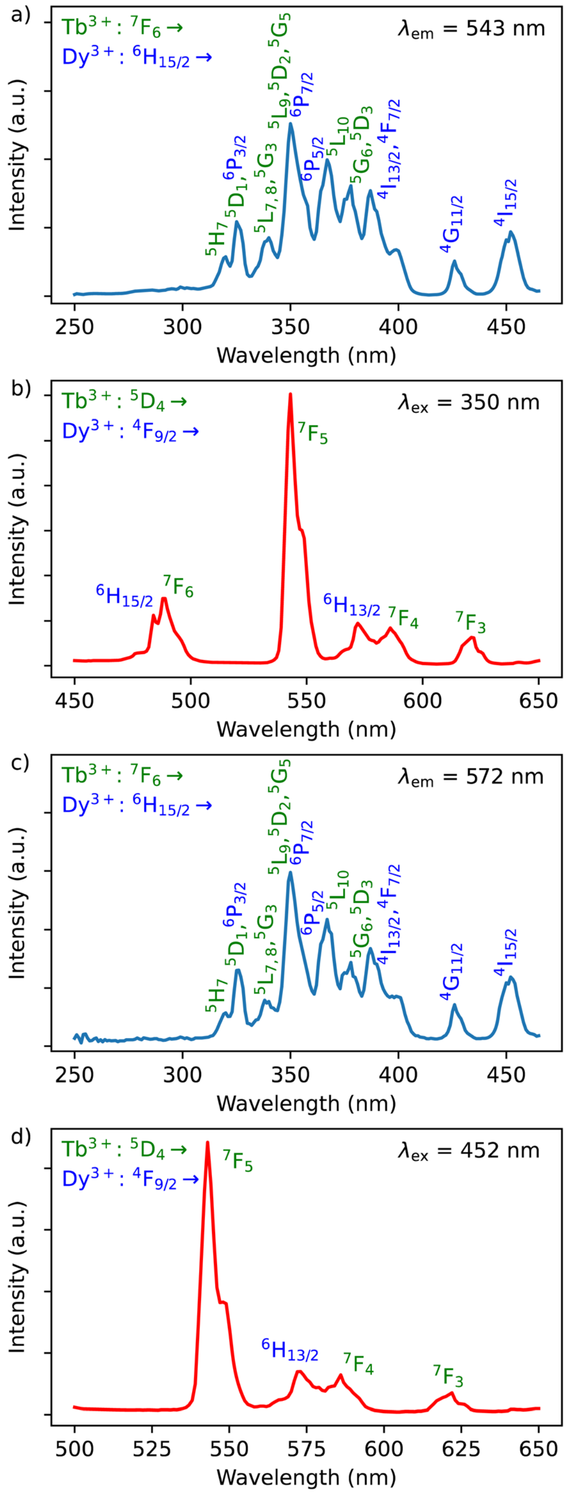

Fig. 6 (a) Excitation spectrum of **2** monitored at $\lambda_{em} = 543$ nm (Tb^{3+} transition) in solid state at room temperature; (b) emission spectra of **2** performed with $\lambda_{ex} = 350$ nm (Tb^{3+} transition) in solid state at room temperature; (c) excitation spectrum of **2** monitored at $\lambda_{em} = 572$ nm (Dy^{3+} transition) in solid state at room temperature; (d) emission spectra of **2** performed with $\lambda_{ex} = 452$ nm (Dy^{3+} transition) in solid state at room temperature. The Tb^{3+} related transitions are notified in green, while Dy^{3+} ones are in blue.

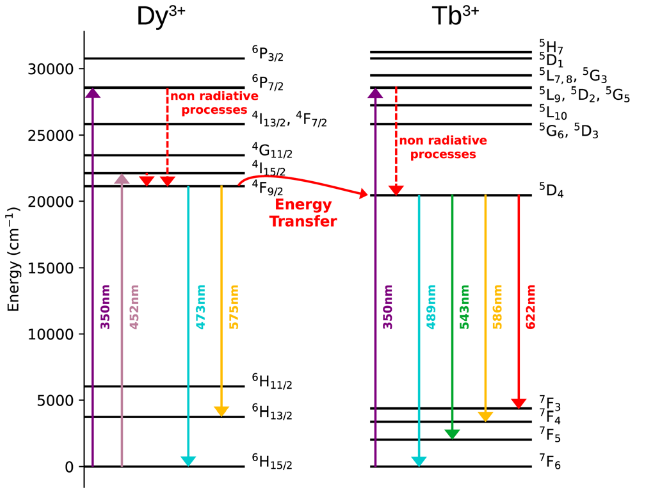

Fig. 7 Simplified energy diagram showing the Dy^{3+} to Tb^{3+} energy transfer.

Luminescence of $Y^{3+}/Tb^{3+}/Eu^{3+}$-compound 3

The excitation spectra of $Tb^{3+}/Eu^{3+}/Y^{3+}$ – containing compound **3** by monitoring the main emission of Eu^{3+} at 612 nm ($^5D_0 \rightarrow {}^7F_2$) and the one of Tb^{3+} at 543 nm ($^5D_4 \rightarrow {}^7F_5$) with the assignment of different transitions characteristic of intra-4f transitions of Eu^{3+} and Tb^{3+} are shown in Fig. 8a and c. The observed transitions are coherent with previously published Tb^{3+}/Eu^{3+}-containing siloxane of similar structure.[34] The maximum intensity of excitation for Eu^{3+} red emission is located at 394 nm, which corresponds to the Eu^{3+} transition $^7F_0 \rightarrow {}^5L_6$. As for Tb^{3+} green emission, the main band is observed at 378 nm, which is attributed to the $^7F_6 \rightarrow {}^5G_6, {}^5D_3$ transitions. The Tb^{3+}-to-Eu^{3+} energy transfer is evidenced by the presence of the Tb^{3+} transition lines in the excitation spectra monitored in the Eu^{3+} emission (at 612 nm).

The emission spectra of **3** were measured under excitations at 394 and 350 nm (Fig. 8b and d). Upon an irradiation at 394 nm, the Eu^{3+} ion is selectively excited to the $^5L_6$ energy level and non-radiative relaxations lead to the population of the $^5D_0$ emitting state (Fig. 8d). The Eu^{3+} transitions are then observed from $^5D_0$ to $^7F_{0-4}$ manifold. Moreover, the excitation at 350 nm (Tb^{3+} band) leads to the main Eu^{3+} emission $^5D_0 \rightarrow {}^7F_{0-4}$ along with the appearance of characteristic Tb^{3+} transitions from $^5D_4$ to $^7F_{2-6}$. This result clearly indicates the occurrence of an intramolecular Tb^{3+}-to-Eu^{3+} energy transfer to the detriment of the Tb^{3+} emission considering the relatively short distances between lanthanides in the core (the shortest direct Ln^{3+}–Ln^{3+} distance in **3** is 3.497 Å and the shortest Ln^{3+}–Ln^{3+} distance through the bridging oxygen atom is 4.625 Å). The corresponding simplified energy diagram showing the Tb^{3+} to Eu^{3+}energy transfer is shown Fig. 9. This observation is in agreement with the previously observed behaviour of Tb^{3+}/Eu^{3+}-containing siloxane.[34] Note that unfortunately, compound **3** does not demonstrated a temperature dependence of its emission useful to establish emissive thermometer.

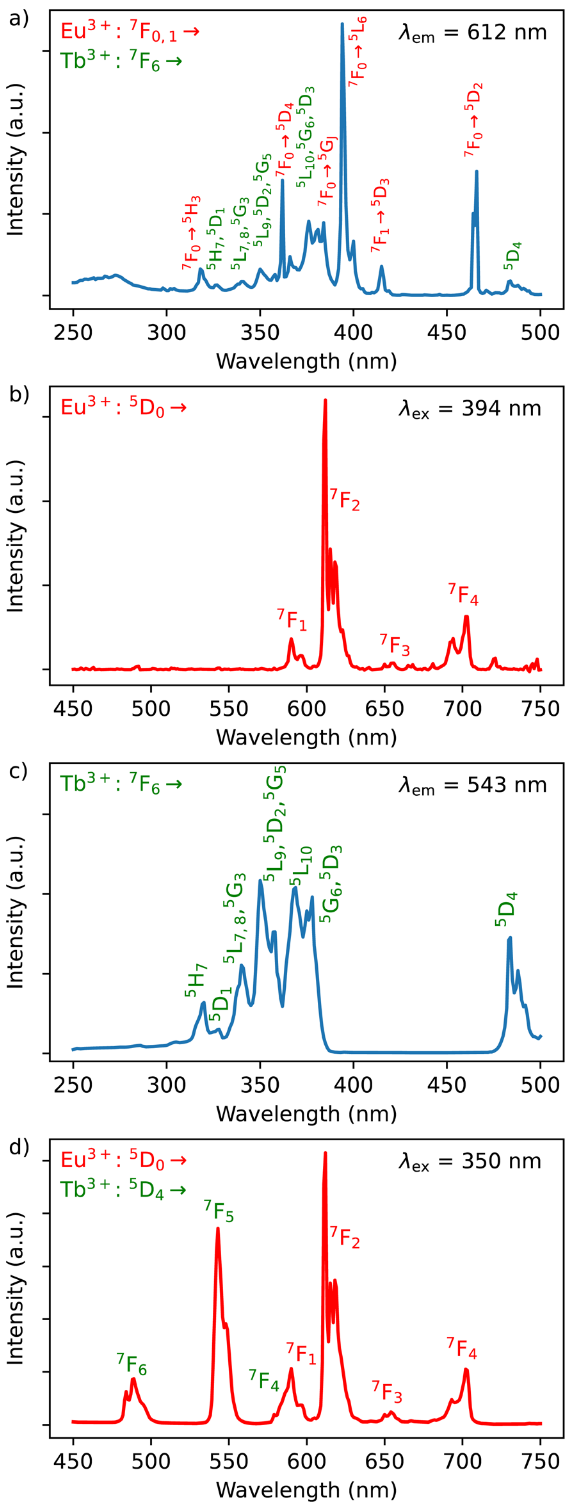

Fig. 8 Solid state excitation spectra of **3** monitored at room temperature at $\lambda_{em} = 612$ nm (Eu^{3+} transition) (a) and at $\lambda_{em} = 543$ nm (Tb^{3+} transition) (c); solid state emission spectra of **3** performed at room temperature with $\lambda_{ex} = 394$ nm (Eu^{3+} transition) (b) and at $\lambda_{ex} = 350$ nm (Tb^{3+} transition) (d). The Tb^{3+} related transitions are notified in green, while Eu^{3+} ones are in red.

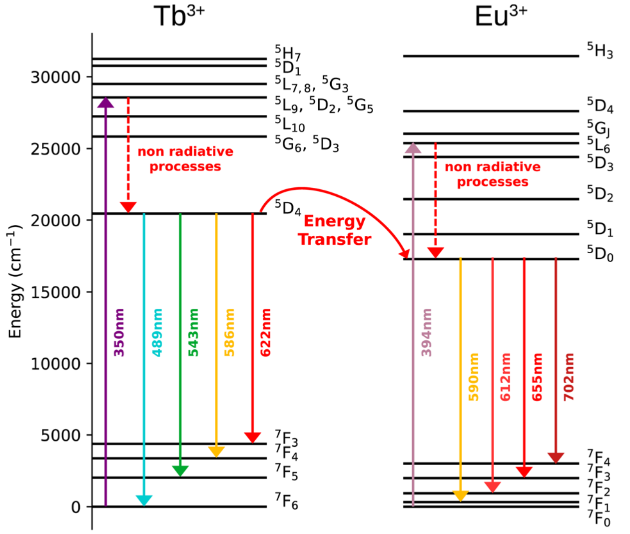

Fig. 9 Simplified energy diagram showing the Tb^{3+} to Eu^{3+} energy transfer.

Conclusions

In summary, we reported a new series of anionic tetranuclear cage-like silsesquioxanes $[NEt_4]_2[(Ph_4Si_4O_8)_2(Ln/Ln')_4(NO_3)_6(EtOH)_2(MeCN)_2]\cdot 4(MeCN)$ containing solid solutions of mixed lanthanide Ln/Ln′ ions Dy^{3+}/Eu^{3+}, Dy^{3+}/Tb^{3+} and $Eu^{3+}/Tb^{3+}/Y^{3+}$ investigating the impact of the lanthanide ions on the magnetic and optical properties. All compounds present prism-like molecular crystal structure where four lanthanide ions are linked through oxygen atoms by forming a core, which is located between two cyclic tetraphenylcyclotetrasiloxanolate moieties. The investigation of their magnetic properties reveals that Dy^{3+}/Eu^{3+} compound **1** presents slow relaxation of the magnetisation under an applied optimal magnetic field of 1000 Oe to partially supress the QTM process, making it a field induced SMM. Note that Dy^{3+}/Tb^{3+} compound **2** does not present the SMM behaviour certainly due to the dipolar interactions between Dy^{3+} ions, which negatively impact the relaxation dynamic. All compounds present lanthanide characteristic luminescence at room temperature. The Eu^{3+} emission of Dy^{3+}/Eu^{3+} compound **1** has been used to establish an original self-referenced thermometry mechanism involving the temperature dependence of the thermal population of low-lying levels of Eu^{3+} situated just above the ground level. The obtained maximum S_r value is equal to 1.15% K^{-1} at 293 K. Therefore, this compound can be considered as a multifunctional field induced SMM and emissive thermometer with a relatively high relative thermal sensitivity (~1% K^{-1}).[9] It represents the third example of Dy^{3+} SMM where slow relaxation of the magnetization is combined with luminescent thermometry in the same compound. Dy^{3+}/Tb^{3+} and $Y^{3+}/Tb^{3+}/Eu^{3+}$ compounds demonstrated a characteristic photoluminescence with the presence of the Dy^{3+} to Tb^{3+} and Tb^{3+} to Eu^{3+} energy transfers, respectively. These results point at significant potential in design of functional metallasesquioxanes[47] including lanthanide centres.[48–50]

Conflicts of interest

There are no conflicts to declare.

Acknowledgements

This research (synthetic and photophysical studies) was funded by the Russian Science Foundation, grant number 22-13-00250. This work (elemental analyses) was in part supported by the Ministry of Science and Higher Education of the Russian Federation (Contract No. 075-03-2023-642) and was performed employing the equipment of Center for Molecular Composition Studies of INEOS RAS. J. L., S. S., G. F. and Y. G. thank the University of Montpellier and CNRS for financial support (project PRC2287 Premium 2019–2021 and IRP "Magnetic and luminescent complexes and cage molecules: from information storage at the molecular scale to nanothermometers"). J. L., S. S., G. F. and Y. G. are grateful to Platform of Analysis and Characterization (PAC) of ICGM for magnetic measurements. J. L. and A. N. K. are grateful for Vernadski program (Embassy of France in Russian Federation). This publication (structural studies) has been supported by the RUDN University Scientific Projects Grant System, project no. 0252392174.

Notes and references

1 F.-S. Guo, B. M. Day, Y.-C. Chen, M.-L. Tong, A. Mansikkamäki and R. A. Layfield, *Science*, 2018, **362**, 1400–1403.

2 K. R. McClain, C. A. Gould, K. Chakarawet, S. J. Teat, T. J. Groshens, J. R. Long and B. G. Harvey, *Chem. Sci.*, 2018, **9**, 8492–8503.

3 C. A. P. Goodwin, F. Ortu, D. Reta, N. F. Chilton and D. P. Mills, *Nature*, 2017, **548**, 439–442.

4 F.-S. Guo, B. M. Day, Y.-C. Chen, M.-L. Tong, A. Mansikkamäki and R. A. Layfield, *Angew Chem. Int. Ed. Engl.*, 2017, **56**, 11445–11449.

5 M. D. Dramićanin, *J. Appl. Phys.*, 2020, **128**, 040902.

6 M. Bettinelli, L. Carlos and X. Liu, *Phys. Today*, 2015, **68**, 38–44.

7 Y. Cui, H. Xu, Y. Yue, Z. Guo, J. Yu, Z. Chen, J. Gao, Y. Yang, G. Qian and B. Chen, *J. Am. Chem. Soc.*, 2012, **134**, 3979–3982.

8 C. D. S. Brites, A. Millán and L. D. Carlos, in *Handbook on the Physics and Chemistry of Rare Earths*, ed. B. Jean-Claude and K. P. Vitalij, Elsevier, 2016, vol. 49, pp. 339–427.

9 C. D. S. Brites, S. Balabhadra and L. D. Carlos, *Adv. Opt. Mater.*, 2019, **7**, 1801239.

10 C. D. S. Brites, P. P. Lima, N. J. O. Silva, A. Millán, V. S. Amaral, F. Palacio and L. D. Carlos, *Nanoscale*, 2012, **4**, 4799–4829.

11 D. Jaque and F. Vetrone, *Nanoscale*, 2012, **4**, 4301–4326.

12 *Luminescence Thermometry: Methods, Materials and Applications – 1st Edition*, **https://www.elsevier.com/books/luminescence-thermometry/dramicanin/978-0-08-102029-6**, accessed June 13, 2022.

13 Y.-S. Ding, T. Han, Y.-Q. Zhai, D. Reta, N. F. Chilton, R. E. P. Winpenny and Y.-Z. Zheng, *Chem.–Eur. J.*, 2020, **26**, 5893–5902.

14 S. K. Gupta, T. Rajeshkumar, G. Rajaraman and R. Murugavel, *Chem. Sci.*, 2016, **7**, 5181–5191.

15 J. Liu, Y.-C. Chen, J.-L. Liu, V. Vieru, L. Ungur, J.-H. Jia, L. F. Chibotaru, Y. Lan, W. Wernsdorfer, S. Gao, X.-M. Chen and M.-L. Tong, *J. Am. Chem. Soc.*, 2016, **138**, 5441–5450.

16 C. Wang, R. Sun, Y. Chen, B.-W. Wang, Z.-M. Wang and S. Gao, *CCS Chem.*, 2020, **2**, 362–368.

17 N. F. Chilton, C. A. P. Goodwin, D. P. Mills and R. E. P. Winpenny, *Chem. Commun.*, 2014, **51**, 101–103.

18 D. N. Woodruff, R. E. P. Winpenny and R. A. Layfield, *Chem. Rev.*, 2013, **113**, 5110–5148.

19 M. Hasegawa, H. Ohmagari, H. Tanaka and K. Machida, *J. Photochem. Photobiol., C*, 2022, **50**, 100484.

20 J.-C. G. Bünzli, *Coord. Chem. Rev.*, 2015, **293–294**, 19–47.

21 G. F. de Sá, O. L. Malta, C. de Mello Donegá, A. M. Simas, R. L. Longo, P. A. Santa-Cruz and E. F. da Silva, *Coord. Chem. Rev.*, 2000, **196**, 165–195.

22 J. Long, Y. Guari, R. A. S. Ferreira, L. D. Carlos and J. Larionova, *Coord. Chem. Rev.*, 2018, **363**, 57–70.

23 J.-H. Jia, Q.-W. Li, Y.-C. Chen, J.-L. Liu and M.-L. Tong, *Coord. Chem. Rev.*, 2019, **378**, 365–381.

24 F. Pointillart, O. Cador, B. Le Guennic and L. Ouahab, *Coord. Chem. Rev.*, 2017, **346**, 150–175.

25 R. Marin, G. Brunet and M. Murugesu, *Angew. Chem., Int. Ed.*, 2021, **60**, 1728–1746.

26 D. Errulat, R. Marin, D. A. Gálico, K. L. M. Harriman, A. Pialat, B. Gabidullin, F. Iikawa, O. D. D. Couto, J. O. Moilanen, E. Hemmer, F. A. Sigoli and M. Murugesu, *ACS Cent. Sci.*, 2019, **5**, 1187–1198.

27 G. Brunet, R. Marin, M.-J. Monk, U. Resch-Genger, D. A. Gálico, F. A. Sigoli, E. A. Suturina, E. Hemmer and M. Murugesu, *Chem. Sci.*, 2019, **10**, 6799–6808.

28 K. Karachousos-Spiliotakopoulos, V. Tangoulis, N. Panagiotou, A. Tasiopoulos, E. Moreno-Pineda, W. Wernsdorfer, M. Schulze, A. M. P. Botas and L. D. Carlos, *Dalton Trans.*, 2022, **51**, 8208–8216.

29 D. A. Gálico, R. Marin, G. Brunet, D. Errulat, E. Hemmer, F. A. Sigoli, J. O. Moilanen and M. Murugesu, *Chem.–Eur. J.*, 2019, **25**, 14625–14637.

30 K. Kumar, D. Abe, K. Komori-Orisaku, O. Stefańczyk, K. Nakabayashi, J. R. Shakirova, S. P. Tunik and S. Ohkoshi, *RSC Adv.*, 2019, **9**, 23444–23449.

31 M. Nie, J. Xiong, C. Zhao, H. Meng, K. Zhang, Y. Han, J. Li, B. Wang, L. Feng, C. Wang and T. Wang, *Nano Res.*, 2019, **12**, 1727–1731.

32 A. N. Kulakova, A. N. Bilyachenko, M. M. Levitsky, V. N. Khrustalev, E. S. Shubina, G. Felix, E. Mamontova, J. Long, Y. Guari and J. Larionova, *Chem.–Eur. J.*, 2020, **26**, 16594–16598.

33 A. N. Kulakova, K. Nigoghossian, G. Félix, V. N. Khrustalev, E. S. Shubina, J. Long, Y. Guari, L. D. Carlos, A. N. Bilyachenko and J. Larionova, *Eur. J. Inorg. Chem.*, 2021, **2021**, 2696–2701.

34 K. Nigoghossian, A. N. Kulakova, G. Félix, V. N. Khrustalev, E. S. Shubina, J. Long, Y. Guari, S. Sene, L. D. Carlos, A. N. Bilyachenko and J. Larionova, *RSC Adv.*, 2021, **11**, 34735–34741.

35 D. A. Gálico, C. M. S. Calado and M. Murugesu, *Chem. Sci.*, 2023, **14**, 5827–5841.

36 *Rigaku Oxford Diffraction, CrysAlisPro*, Version 1.171.41.106a.

37 A. L. Spek, *PLATON, A Multipurpose Crystallographic Tool*, Utrecht University, The Netherlands, https://slideplayer.com/slide/8528251/, accessed February 8, 2023.

38 G. M. Sheldrick, *Acta Crystallogr., Sect. C: Struct. Chem.*, 2015, **71**, 3–8.

39 S. T. Liddle and J. van Slageren, *Chem. Soc. Rev.*, 2015, **44**, 6655–6669.

40 K. Binnemans, *Coord. Chem. Rev.*, 2015, **295**, 1–45.

41 L. Zhao, J. Cai, F. Hu, X. Li, Z. Cao, X. Wei, Y. Chen, M. Yin and C.-K. Duan, *RSC Adv.*, 2017, **7**, 7198–7202.

42 A. Bednarkiewicz, L. Marciniak, L. D. Carlos and D. Jaque, *Nanoscale*, 2020, **12**, 14405–14421.

43 V. Trannoy, A. N. Carneiro Neto, C. D. S. Brites, L. D. Carlos and H. Serier-Brault, *Adv. Opt. Mater.*, 2021, **9**, 2001938.

44 Ravita and A. S. Rao, *J. Lumin.*, 2021, **239**, 118325.

45 J. Juárez-Batalla, A. N. Meza-Rocha, H. G. Muñoz and U. Caldiño, *Opt. Mater.*, 2017, **64**, 33–39.

46 M. Vijayakumar, K. Viswanathan and K. Marimuthu, *J. Alloys Compd.*, 2018, **745**, 306–318.

47 M. M. Levitsky, Y. V. Zubavichus, A. A. Korlyukov, V. N. Khrustalev, E. S. Shubina and A. N. Bilyachenko, *J. Cluster Sci.*, 2019, **30**, 1283–1316.

48 (*a*) P. Wytrych, J. Utko, M. Stefanski, J. Kłak, T. Lis and Ł. John, *Inorg. Chem.*, 2023, **62**, 2913–2923; (*b*) G. Félix, A. Kulakova, S. Sene, C. Charlot, A. N. Bilyachenko, A. A. Korlyukov, A. D. Volodin, E. S. Shubina, I. G. Elizbarian, Y. Guari and J. Larionova, *Organometallics*, 2023, DOI: 10.1021/acs.organomet.3c00009.

49 K. Sheng, W.-D. Si, R. Wang, W.-Z. Wang, J. Dou, Z.-Y. Gao, L.-K. Wang, C.-H. Tung and D. Sun, *Chem. Mater.*, 2022, **34**, 4186–4194.

50 K. Sheng, R. Wang, A. Bilyachenko, V. Khrustalev, M. Jagodič, Z. Jagličić, Z. Li, L. Wang, C. Tung and D. Sun, *ChemPhysMater*, 2022, **1**, 247–251.